



Experimental and numerical investigation of fracture in a cast aluminium alloy

E. Fagerholt^{a,*}, C. Dørum^{a,b}, T. Børvik^{a,c}, H.I. Laukli^{a,d}, O.S. Hopperstad^a

^a Structural Impact Laboratory (SIMLab), Centre for Research-based Innovation (CRI) and Department of Structural Engineering, Norwegian University of Science and Technology, Rich. Birkelands vei 1A, NO-7491 Trondheim, Norway

^b SINTEF Materials and Chemistry, Rich. Birkelands vei 2B, NO-7465 Trondheim, Norway

^c Norwegian Defence Estates Agency, Research and Development Department, PB 405, Sentrum, NO-0103 Oslo, Norway

^d Norsk Hydro ASA, Research and Technology Development, NO-6600 Sunndalsøra, Norway

ARTICLE INFO

Article history:

Received 23 February 2010

Received in revised form 12 August 2010

Available online 17 August 2010

Keywords:

Arcan tests

Digital image correlation

Crack propagation

Stochastic variation

Element erosion

ABSTRACT

This paper describes an experimental and numerical investigation on the fracture behaviour of a cast AlSi9MgMn aluminium alloy. In the experiments, a modified Arcan test set-up was used to study mixed-mode fracture. During testing, the tension load and the displacement of the actuator of the test machine were recorded, simultaneously as a high-resolution digital camera was used to record a speckle-patterned surface of the specimen. The recorded images were post-processed using an in-house digital image correlation (DIC) software to obtain information of the displacement and strain fields in the specimen during the test. In addition, some newly implemented features in the DIC software allowed us to detect and follow the crack propagation in the material. The numerical calculations were carried out with a user-defined material model implemented in an explicit finite element code. In the model, the material behaviour is described by the classical J_2 flow theory, while fracture was modelled by the Cockcroft–Latham criterion, assuming the fracture parameter to follow a modified weakest-link Weibull distribution. With the proposed probabilistic fracture modelling approach, the fracture parameter can be introduced as a random variable in the finite element simulations. Crack propagation was modelled by element erosion, and a non-local damage formulation was used to reduce mesh-size sensitivity. To reveal the effect of mesh density and meshing technique on the force–displacement curves and the crack propagation, several different meshes were used in the numerical simulations of the modified Arcan tests. The numerical results were finally compared to the experimental data and the agreement between the measured and predicted response was evaluated.

© 2010 Published by Elsevier Ltd.

1. Introduction

In design of thin-walled structural components for ultimate or accidental loads, it is important to evaluate the risk of failure by buckling for compressive loads and necking and fracture for tensile loads. Several approaches may be used to describe fracture in thin-walled components. In a recent paper, Mediavilla et al. (2006) distinguished between three approaches for modelling fracture in finite element analysis, namely the discontinuous, continuous and combined approaches. In the discontinuous approach, the geometry of the crack is modelled explicitly, i.e. the finite element model includes a strong discontinuity. The cohesive zone method (e.g. Needleman, 1990; Scheider and Brocks, 2006) and the extended finite element method (e.g. Moës et al., 1999; Song et al., 2008) are examples of the discontinuous approach. In the continuous approach, the degradation of the material in the fracture process

zone is described by a constitutive model, while cracks are described by continuous regions that have altogether lost their load-carrying capacity due to damage softening (Mediavilla et al., 2006). Examples of the continuous approach are porous plasticity (e.g. Gurson, 1977; Rousselier, 1987) and continuum damage mechanics (e.g. Lemaitre, 1992). The combined continuous–discontinuous approach consists of modelling the degradation in the process zone by porous plasticity or continuum damage mechanics and then introducing a strong discontinuity for instance at a given porosity or a critical damage. Mediavilla et al. (2006) proposed an uncoupled continuous–discontinuous approach, where the damage in the fracture process zone is computed but its influence on the material behaviour is neglected. The ductile damage variable was then used as an indicator for crack initiation and propagation, while an advanced remeshing and node-splitting approach was developed for predicting crack propagation.

Digital image correlation (DIC) has been an increasingly popular and applicable tool, the last decades for gaining information about displacement and strain fields in mechanical experiments (Rastogi, 2000). Traditionally, the measurements of these field properties have been limited to specimens or regions of interest experiencing

* Corresponding author. Tel.: +47 73 59 46 93; fax: +47 73 59 47 01.

E-mail address: egil.fagerholt@ntnu.no (E. Fagerholt).

continuous displacement fields. Trying to implement DIC field measurements in experiments where specimens undergo crack propagation, opens up to a series of new challenges depending on the application. Usually a significant amount of manual interaction is needed to deal with a propagating crack which may have different properties from experiment to experiment. With the ongoing technical revolution in digital cameras, particularly when it comes to image resolution and frame rate, huge amount of data may be generated from a single mechanical experiment. This facilitates better resolution and accuracy in DIC measurements. However, manual interaction becomes less desirable. Typical challenges using DIC in experiments involving crack propagation are automatic handling and modelling of a growing crack through the measured area of the specimen. A number of studies regarding these topics have been presented. Helm (2008) published a procedure for automatic handling of multiple growing cracks in a concrete specimen using the Newton–Raphson based DIC process, while R  thor   et al. (2007) showed how the discontinuity in the displacement field caused by a crack can be modelled by using enrichment of nodal degrees of freedom in an “extended finite element” DIC process (X-DIC). However, the analysis of propagating cracks in a specimen is still considered a challenging task when it comes to automatic detection and handling of the discontinuous displacement field. In this study, an automatic crack detection and handling technique, developed and presented by Fagerholt et al. (in preparation), was used in combination with a “finite element” DIC algorithm to analyze images of specimens experiencing crack propagation in mechanical experiments.

The fracture behaviour of cast aluminium alloys has been studied by e.g. Mohr and Henn (2007) and Teng et al. (2008). In these studies, experiments in combined tension and shear loading were conducted. Combining the experimental results with finite element simulations, the fracture strain as a function of stress triaxiality (fracture locus) was established for the material. In this paper, we have studied the fracture behaviour of thin-walled cast aluminium components experimentally and numerically. The cast components had U-shaped geometry with wall thickness 2.5 mm. Samples were cut from the component walls for testing under quasi-static loading conditions in a modified Arcan test set-up (Amstutz et al., 1996; Amstutz et al., 1997; Arcan et al., 1978), which facilitated mixed-mode fracture experiments by varying the orientation of the sample in the fixture. The cast components were made of the aluminium alloy AlSi9MgMn which has applications in automotive components. The material behaviour of the cast components has previously been thoroughly characterized by D  rum et al. (2009). Large variations in tensile ductility between parallel tests were found, and a probability distribution of the tensile ductility was established.

During testing, a high-resolution digital camera was used to record a speckle-pattern on the surface of the sample, and the recorded images were post-processed using an in-house DIC software to obtain the displacement and strain fields in the sample. Some newly implemented features in the DIC software allowed us to detect and follow the crack propagation in the sample, which is essential for assessment of numerical methods for predicting fracture and crack propagation. The numerical calculations were carried out with the commercial explicit finite element code LS-DYNA (LSTC, 2003) using shell elements and an uncoupled continuous–discontinuous approach to describe crack propagation. The classical J_2 flow theory was adopted to describe the material behaviour, the damage evolution in the fracture process zone was computed according to the Cockcroft–Latham criterion (Cockcroft and Latham, 1968), while element erosion was used to model the crack propagation. The fracture parameter was assumed to follow a modified weakest-link Weibull distribution and introduced as a random variable in the finite element simulations. This

was done to account for the scatter found in the tensile ductility of the AlSi9MgMn alloy. A non-local damage formulation was adopted to reduce mesh-size sensitivity. To reveal the effect of mesh density and meshing technique on the force–displacement curves and crack propagation, several different meshes were used in the numerical simulations of the modified Arcan tests. The numerical results were finally compared to the measured data. It will be shown that good agreement is in general obtained between the measured and predicted response.

2. Material

All castings were produced with an AlSi9MgMn alloy using Hydro Aluminium’s high pressure die casting (HPDC) machine dedicated for aluminium alloy research. The machine is a B  hler shot-controlled development machine with a locking force of 4.1 MN. An illustration of a casting with gating system and vacuum channels is shown in Fig. 1. The castings were produced without vacuum in the present investigations. The casting has a generic U-shaped geometry with 2.5 mm wall thickness. Details of the alloy composition and the HPDC production parameters are provided in D  rum et al. (2009). Fig. 2 shows the typical microstructure of the AlSi9MgMn alloy in T1-condition.

Flat dogbone specimens were machined from the wide web, the inlet wall and the outlet wall of the cast U-profiles in Fig. 1. A total of 30 specimens were tested under quasi-static tensile loading conditions using 10 parallel tests from each part of the U-profile. The strain rate during the tests was approximately $2 \times 10^{-3} \text{ s}^{-1}$. The specimens were aligned with the longitudinal direction of the cast component. It is referred to D  rum et al. (2009) for a complete description of the material characterization (including uniaxial tension, notched tension, shear and plate bending tests) of the AlSi9MgMn alloy.

As expected in T1 condition, most of the test specimens were found to fail before the point of diffuse necking. Typical work-hardening curves in terms of Cauchy stress and logarithmic plastic strain are provided in Fig. 3 for different parts of the component. It is observed that the material in the outlet wall is far less ductile than the material in the inlet wall and the web. The work-hardening curves are represented in parametric form

$$\sigma = \sigma_0 + \sum_{i=1}^2 Q_i (1 - \exp(-C_i \epsilon^p)), \quad (1)$$

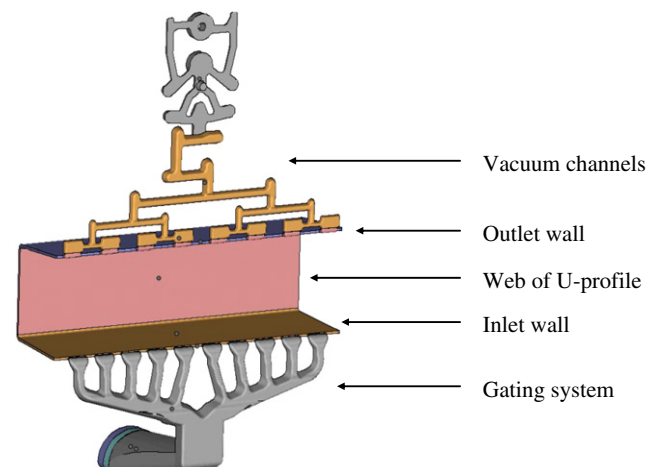


Fig. 1. Illustration of the U-profile casting with gating and vacuum channels. The length of the profile is 300 mm, the web 90 mm and the walls 75 mm. The thickness is 2.5 mm.

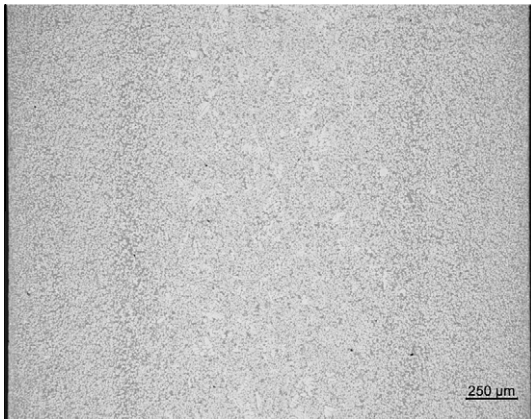


Fig. 2. Typical through-thickness microstructure of HPDC AlSi9MgMn in T1-condition taken from the outlet wall of the casting. Note that the darkest grey phase exhibits Al-Si eutectic.

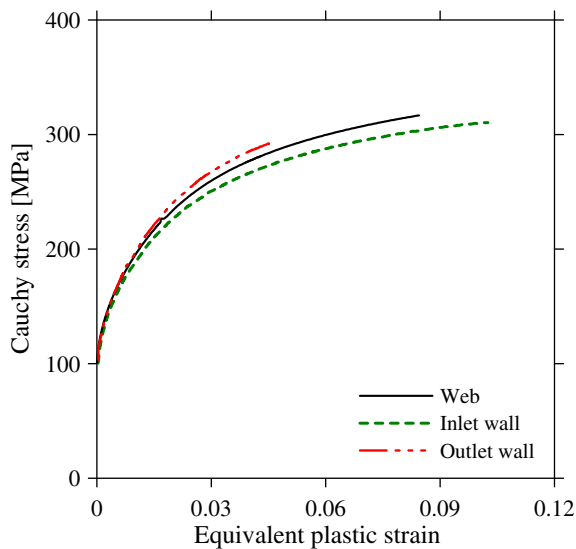


Fig. 3. Typical Cauchy stress versus equivalent (or logarithmic) plastic strain curves obtained from uniaxial tensile tests of AlSi9MgMn. Note that fracture occurs prior to necking in all tests.

where σ is the Cauchy stress, ε^p is the logarithmic plastic strain, σ_0 is the proportionality limit, and Q_1 and C_1 are hardening parameters. A least squares method was used to determine the parameters of this equation for each of the experimental work-hardening curves. It is noted that in uniaxial tension, the equivalent plastic strain equals the logarithmic plastic strain. Material parameters representing the mean work-hardening curve of the web are given in Table 1.

As seen from Fig. 3, the difference in measured values of fracture strain is significant for specimens cut from different parts of the profile. The largest scatter is found for the specimens cut from the outlet wall. The material in the inlet wall of the casting is in average significantly more ductile than the material in the web and the outlet wall of the component. It should be noted that the

scatter in yield stress and work-hardening is relatively low (Dørum et al., 2009).

Several defects, some of which are inherent to the HPDC process, play a role in the mechanical performance of die-castings. Macro-segregation of eutectic, intermetallic particles (Laukli et al., 2005) and primary α -Al crystals (Laukli et al., 2005), porosity (Gourlay et al., 2007), oxide bifilms (Campbell, 2005) and confluence welds (Campbell, 1988) are addressed as typical HPDC defects. It is thus not possible to point out a single defect controlling the mechanical performance. The works by Gokhale and Patel (2005) and Gokhale and Patel (2005) on the mechanical properties of cast aluminium alloys showed that there is a strong quantitative correlation between the area fraction of defects and the tensile ductility. For a tilt-pour-permanent mould cast aluminium alloy the controlling defects were identified as oxide films and shrinkage pores, while for a semi-solid metal cast aluminium alloy the controlling defects were essentially residues of modifiers, fluxes, grain refiners and mould release agents. When looking at the attractive features of a HPDC microstructure, it is well known that a very fine-grained (grain size of less than 10 μm) and commonly defect-free surface layer is important for the mechanical properties. The surface layer, up to several hundred microns thick, forms due to the very high cooling rate in HPDC.

3. Experimental set-up

3.1. Modified Arcan tests

Fig. 4 illustrates the experimental set-up used in this study, which is based on Arcan et al. (1978) and Voloshin and Arcan (1980). The set-up consists of two rigid steel platens and a notched butterfly specimen. The geometry and dimensions of the specimen are shown in Fig. 5. The specimen is connected to the steel platens using 12 M6-bolts and the assembly is mounted in a standard servo-hydraulic tensile machine using bolted connections. As indicated in Fig. 4, the orientation of the specimen may be changed to obtain different loading angles β . Changing the loading angle, mode I is obtained for $\beta = 90^\circ$, mode II for $\beta = 0^\circ$, while other loading angles give mixed modes. This feature of the test set-up facilitates studies of mixed-mode fracture. Since the fixtures are loaded through single pins on each side, see Fig. 4, they are allowed to rotate during displacement. This rotation may lead to lateral displacements of the fixtures which affect the loading of the specimen. Prior to the test, one side of the specimen was spray-painted with a combination of black and white paint, giving a fine-grained and high-contrast speckle-pattern (see e.g. Fig. 8) required to enhance the optical measurements. The test series conducted in this study consisted of 5, 5 and 4 tests with β equal to 0° , 45° and 90° , respectively.

During a test, the tension load and the displacement of the hydraulic actuator were recorded at a rate of 15 Hz. In addition, 8-bit grey-scale images of the speckle-patterned specimen surface were recorded at a frame rate of 10 Hz using a Prosilica GC2450 digital camera equipped with a 28–105 mm Nikon lens. The spatial resolution of the recorded images was 2448×2050 pixels. The recorded images were post-processed using an in-house digital image correlation (2D-DIC) software (Fagerholt et al., in preparation), obtaining information on displacement and strain fields as well as information on the crack propagation in the specimen. The camera was pre-arranged with its optical axis normal to the specimen surface. A linear relationship between coordinates on the specimen surface and the image coordinates was assumed in the 2D-DIC analysis. The spatial resolution of the image recordings are calculated to 0.03 mm/pixels and the “finite element” size used in the 2D-DIC analysis is 32 pixels or 0.96 mm.

Table 1
Work hardening parameters representing the mean curve of the web.

Alloy	Position	σ_0 (MPa)	Q_1 (MPa)	C_1	Q_2 (MPa)	C_2
AlSi9MgMn	Web	104.8	39.6	373.2	181.2	33.2

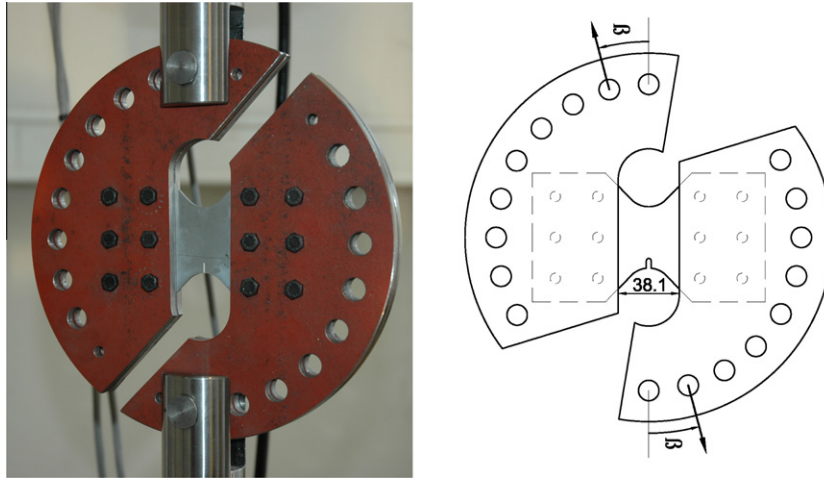


Fig. 4. Picture with $\beta = 0^\circ$ (left) and sketch (right) of the Arcan test set-up.

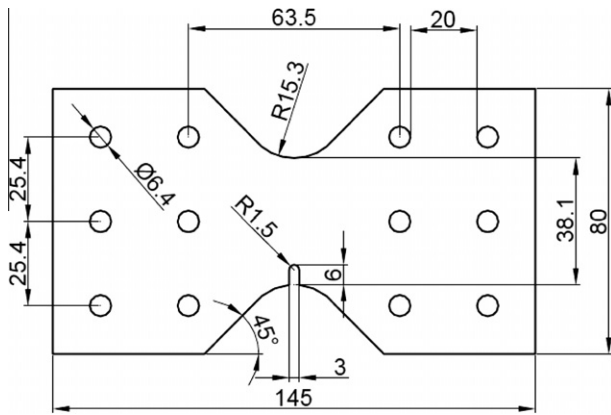


Fig. 5. Geometry and dimensions of notched butterfly test specimen (in mm).

3.2. Digital image correlation (2D-DIC) measurements

The post-processing procedures of the images were based on the “finite element” digital image correlation procedure proposed by Besnard et al. (2006), where the displacement fields are calculated by carrying out a global optimization of the nodal displacements in a mesh of Q4 elements. The DIC algorithm is essentially based on the conservation of optical flow, which limits the algorithm to continuous displacement fields. Discontinuities in the displacement field, such as cracks propagating through the specimen, may cause the solution to diverge and give erroneous results. To overcome the problem of propagating cracks, modifications to the DIC algorithm are implemented. These modifications consist of automatic detection and handling of crack propagation. The details of this technique have been presented in Fagerholt et al. (in preparation).

The automatic detection of cracks is based on statistical evaluation of grey-scale correlation residuals with a set of predefined levels. Based on this evaluation a weight map is generated, giving each pixel inside the correlation region a weight factor between 0 and 1. The weight factor indicates the quality of the correlation in the corresponding pixel. A pixel with weight factor 0 is totally disregarded in the DIC optimization procedure, while a pixel with weight factor 1 is fully contributing to the correlation. Typically a pixel located in an area where a crack is present, should not be part of the correlation and is given a weight factor 0. The introduction of this weight factor map helps the DIC optimization algorithm to converge to the correct solution of the displacement field, even

for large propagating cracks, because the pixels located in a cracked region are “weighted out” of the solution.

The final step of handling crack propagating in the DIC algorithm is to carry out modifications to the mesh so that the elements (and the displacement field) are not defined in the cracked region. In this study, this is carried out by mesh adaptivity, motivated by the techniques developed for the finite element method. Based on predefined levels, elements which contain a high degree of low-weighted pixels are refined (split in four new smaller elements) or eroded (completely removed from the solution).

The crack handling procedure described above, with properly adjusted predefined levels for weight factor map generation and mesh adaptivity, helps the DIC optimization algorithm to calculate the continuous displacement field in the parts of the specimen not affected by the crack. In Section 4, example images from tests with the calculated strain fields plotted on top of the image will be given. It can then be seen that the strain field is not defined in the cracked area, due to the erosion of elements in this region. The reader is again referred to Fagerholt et al. (in preparation) for further details on the DIC procedures used in these experiments.

4. Experimental results

A total of 14 successful notched butterfly tests were carried out varying the loading angle β between 0° , 45° and 90° . Displacement, force and digital images were recorded for all tests. The images were post-processed using the previously described DIC algorithm to obtain the two-dimensional displacement and strain fields of the specimen surface.

Fig. 6 illustrates the force–displacements curves for these 14 tests. The figure shows that significant scatter between replicate tests appears, which is consistent with the scatter found in the tensile tests presented in Dørum et al. (2009). Note that the displacement and force measurements in the plots of Fig. 6 were taken directly from the linear transducer and the load cell of the testing machine. In contrast, later plots will use displacement measurements from the DIC analysis. Fig. 7 shows the reference points on the specimen used in the DIC analysis to obtain an overall measure of the specimen’s deformation. Let w_x and w_y denote the x - and y -components of the relative displacement between points 1 and 2. For $\beta = 0^\circ$, w_x is taken as a measure of overall deformation, while for $\beta = 45^\circ$ and $\beta = 90^\circ$ the overall deformation is defined by $w = \sqrt{w_x^2 + w_y^2}$. The same procedure is used to extract the overall deformation in the finite element analysis presented in Section 5.

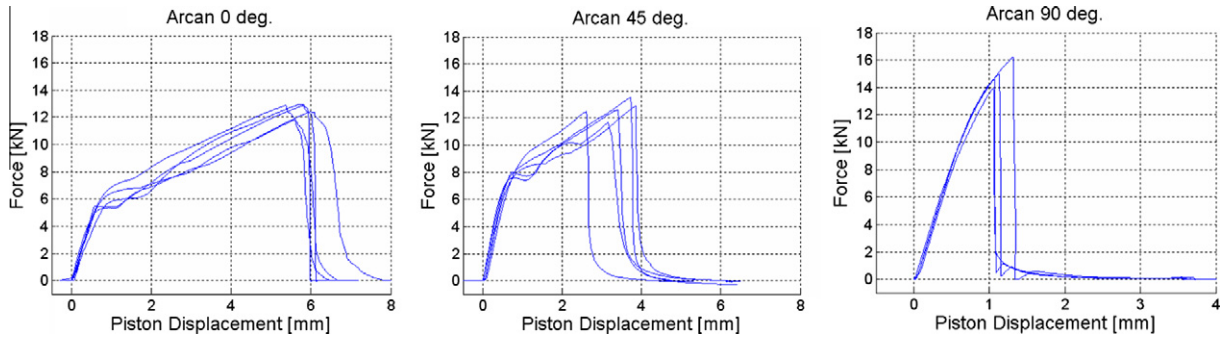


Fig. 6. Force–displacement curves for the 14 experiments for (from left to right) $\beta = 0^\circ, 45^\circ$ and 90° .

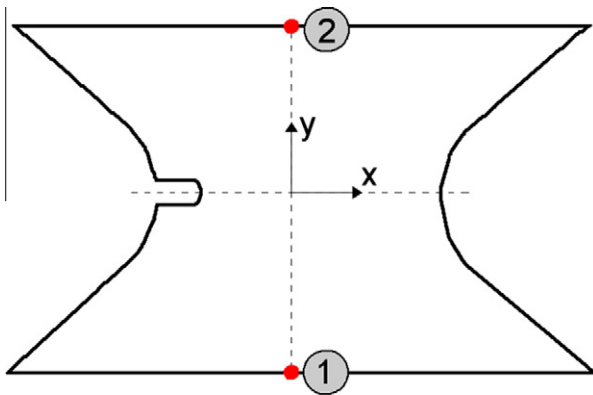


Fig. 7. Definition of measured relative displacements from the DIC analysis.

Fig. 8 shows a set of selected images from a test with $\beta = 45^\circ$. The propagating crack can clearly be seen in the images. Typical examples of crack paths from replicate tests with β equal to $0^\circ, 45^\circ$ and 90° are shown in Fig. 9. Except maybe for $\beta = 90^\circ$ (i.e. mode I fracture), there are apparent differences in the crack path between the replicates. It can also be seen that slant fracture occurs through the thickness in all tests. It is noted that two of the specimens loaded in mode II exhibits a kinked crack. The reason for this may be the small rotations of the fixtures during displacement, as

discussed in Section 3.1, which implies that the configuration is not exactly mode II.

Based on the two-dimensional displacement field $\mathbf{u} = \mathbf{u}(\mathbf{X}, t)$ generated by the DIC analysis, where \mathbf{X} are the material coordinates and t is time, the deformation gradient $\mathbf{F} = \mathbf{F}(\mathbf{X}, t)$ is calculated as

$$\mathbf{F} = \frac{\partial \mathbf{x}}{\partial \mathbf{X}} = \mathbf{1} + \frac{\partial \mathbf{u}}{\partial \mathbf{X}}, \quad (2)$$

where $\mathbf{x}(\mathbf{X}, t) = \mathbf{X} + \mathbf{u}(\mathbf{X}, t)$ are the spatial coordinates of the material point \mathbf{X} and $\mathbf{1}$ is the second-order identity tensor. The Green deformation tensor $\mathbf{C} = \mathbf{C}(\mathbf{X}, t)$ is then calculated as

$$\mathbf{C} = \mathbf{F}^T \mathbf{F}. \quad (3)$$

The in-plane principal stretches $\mu_i = \mu_i(\mathbf{X}, t)$, $i = 1, 2$, are found by solving the eigenvalue problem for the Green deformation tensor

$$(\mu_i^2 \mathbf{1} - \mathbf{C}) \cdot \mathbf{n}_i = \mathbf{0}, \quad (4)$$

where \mathbf{n}_i are the principal directions of \mathbf{C} . The logarithmic principal strains $\varepsilon_i = \varepsilon_i(\mathbf{X}, t)$, $i = 1, 2$, are then calculated as

$$\varepsilon_i = \ln(\mu_i). \quad (5)$$

Assuming negligible elastic strains and plastic incompressibility, the logarithmic principal strain in the thickness (out-of-plane) direction is estimated as

$$\varepsilon_3 = -(\varepsilon_1 + \varepsilon_2). \quad (6)$$

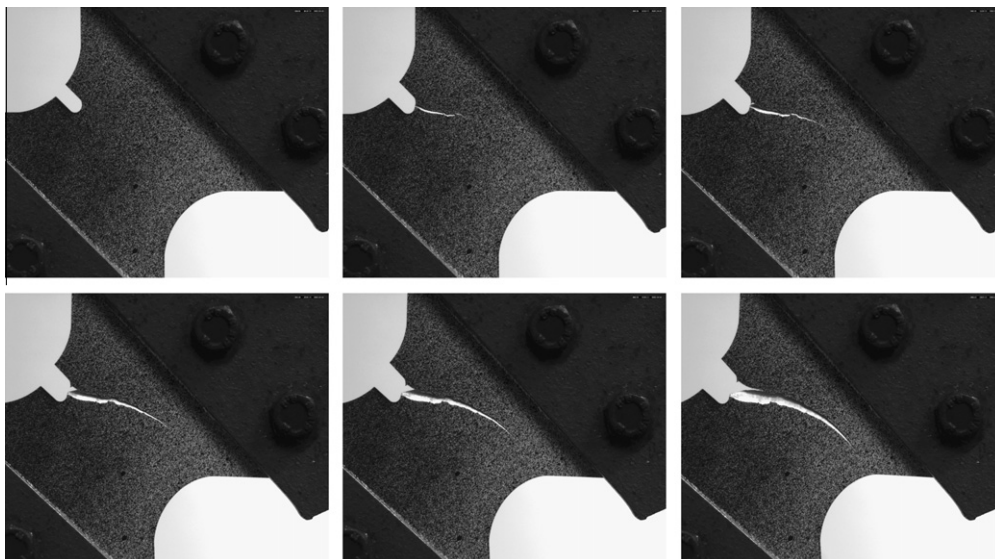


Fig. 8. Recorded images from a modified Arcan test for $\beta = 45^\circ$, showing the development of the crack path during the test.

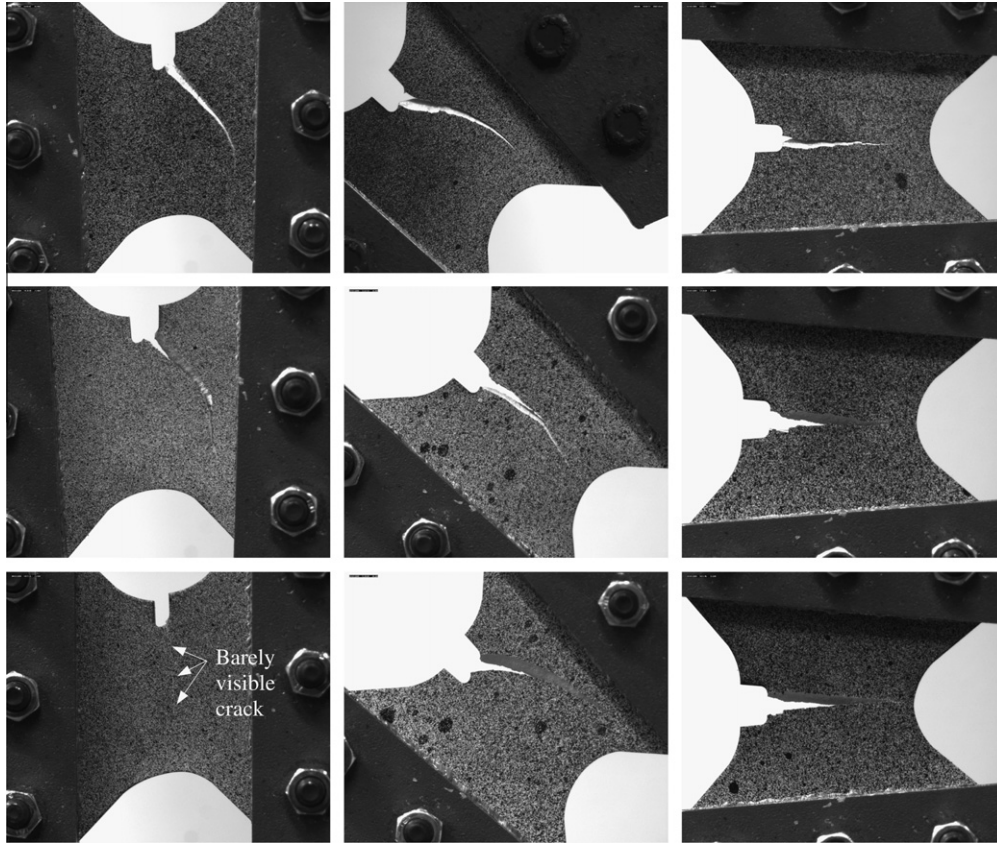


Fig. 9. Crack paths from three replicate tests (top–down). From left to right $\beta = 0^\circ$, 45° and 90° .

An effective strain measure $\varepsilon_{eff} = \varepsilon_{eff}(\mathbf{X}, t)$ is defined according to

$$\varepsilon_{eff} = \sqrt{\frac{2}{3}(\varepsilon_1^2 + \varepsilon_2^2 + \varepsilon_3^2)} = \sqrt{\frac{4}{3}(\varepsilon_1^2 + \varepsilon_1\varepsilon_2 + \varepsilon_2^2)}, \quad (7)$$

where Eq. (6) was used to obtain the latter equality. It is noted that ε_{eff} represents the norm of the total strain tensor, and should not be confused with the equivalent plastic strain (here denoted ε_{eq}) used to describe work-hardening in the constitutive model in Section 5.

Figs. 10–12 show the evolution of the calculated effective strain field $\varepsilon_{eff} = \varepsilon_{eff}(\mathbf{X}, t)$ in three of the performed tests plotted on top of the corresponding images for $\beta = 0^\circ$, 45° and 90° . Note that the colour scaling in these figures is logarithmic due to the exponential spatial variation of the effective strain in the specimens. It should also be noted that the strain calculations are based on the DIC “finite element” size of 32 pixels (0.96 mm) which sets limitations to the strain calculations, especially around the notch where high strain gradients are present. Fig. 13 gives the corresponding force–displacement curves for the experiments shown with effective strain maps in Figs. 10–12. The instants of the strain maps in Figs. 10–12 have been noted with a numbers 1–6 in the force–displacement curves in Fig. 13. The results show that different force–displacement response and fracture mode are obtained by varying the loading angle. It is particularly noted that the fracture is much more abrupt for $\beta = 90^\circ$ (mode I) than for the other load cases. This is evident in Fig. 13 for $\beta = 90^\circ$ where the time interval between points 4 and 5 equals the frame rate of 10 Hz. Fig. 14 illustrates the correlation grey-scale residual maps at a late stage in tests with β equal to 0° , 45° and 90° , respectively. Due to the poor correlation in the crack region, the residuals become high and the residual map can be used to view the crack path in material coordinates.

5. Finite-element models

The numerical simulations of the modified Arcan tests were carried out with an user-defined material model implemented in the commercial explicit FE-code LS-DYNA. The load is applied to the test specimen as a prescribed rigid body motion in the loading direction of the steel plate support. The rigid steel plate supports can rotate in-plane around the pinned connections, allowing for lateral displacements. In the model, the material behaviour is described by the classical J_2 flow theory, i.e. an elastic–plastic constitutive model including the von Mises yield criterion, the associated flow rule and isotropic hardening. Fracture is modelled by the Cockcroft–Latham criterion (Cockcroft and Latham, 1968), assuming the fracture parameter to follow a modified weakest-link Weibull distribution (Dørum et al., 2009; Dørum et al., 2009; Weibull, 1951). With the present probabilistic fracture modelling approach, the fracture parameter can be introduced as a random variable in the finite element simulations. More details about the implemented user-defined material model are given by Dørum et al. (2009).

The yield function is defined by

$$f(\boldsymbol{\sigma}, \varepsilon_{eq}) = \sigma_{eq}(\boldsymbol{\sigma}) - \sigma_Y(\varepsilon_{eq}) = 0, \quad (8)$$

where $\boldsymbol{\sigma}$ is the Cauchy stress tensor, σ_{eq} is the von Mises equivalent stress and ε_{eq} is the corresponding equivalent plastic strain. The flow stress σ_Y is defined by the isotropic hardening rule given by Eq. (1), and the corresponding work-hardening parameters provided in Table 1. This implies that any variation in flow stress with position in the casting was not accounted for in the simulations. The Cockcroft–Latham fracture criterion is adopted

$$W = \int_0^{\varepsilon_{eq}} \max(\sigma_1, 0) d\varepsilon_{eq} \leq W_c, \quad (9)$$

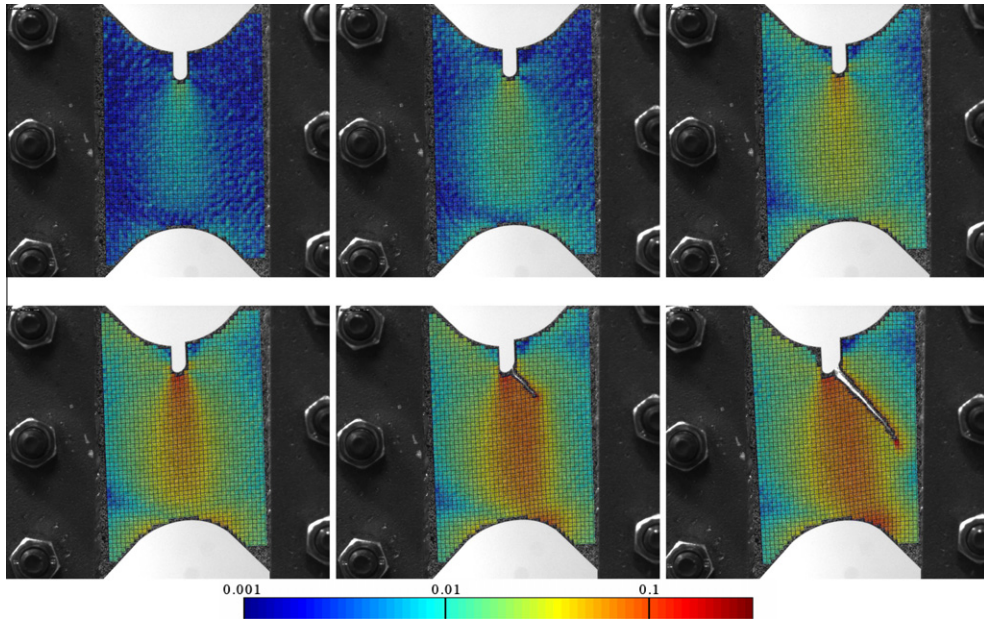


Fig. 10. Measured effective strain fields for a selection of images in a test for $\beta = 0^\circ$ (mode II). The strain fields are plotted on top of the recorded images in current configuration as logarithmic scaled colour maps.

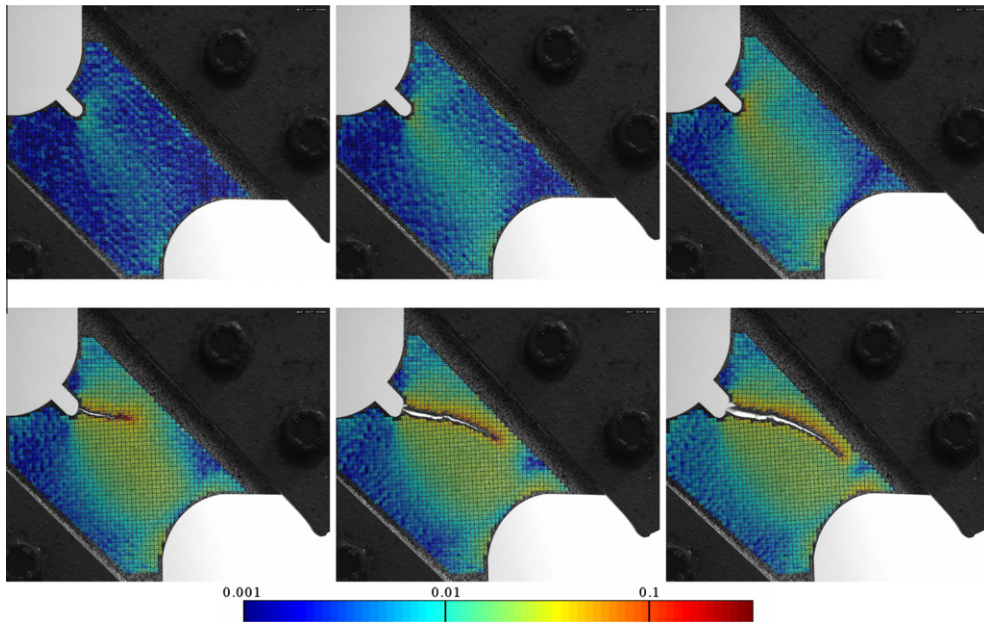


Fig. 11. Measured effective strain fields for a selection of images in a test for $\beta = 45^\circ$ (mixed-mode). The strain fields are plotted on top of the recorded images in current configuration as logarithmic scaled colour maps.

where W is denoted the Cockcroft–Latham integral, σ_1 is the maximum principal stress, and W_c is the critical value of the integral W at which fracture occurs. It is convenient to re-write this fracture criterion as a damage evolution law in the form

$$\dot{D} = \begin{cases} \frac{\sigma_1}{W_c} \dot{\varepsilon}_{eq} & \text{for } \sigma_1 > 0, \\ 0 & \text{for } \sigma_1 \leq 0, \end{cases} \quad (10)$$

where D is the damage variable. Fracture occurs when D equals unity. As the Cockcroft–Latham fracture criterion is based upon only one parameter, a single material test is sufficient for the calibration. In the present study, the fracture parameter was identified from uniaxial tension tests ($\sigma_1 > 0$) as

$$W_c = \int_0^{\varepsilon_f} \sigma_1 d\varepsilon_{eq}, \quad (11)$$

where ε_f is the fracture strain. Note that fracture occurs without any sign of necking for the actual material, thus facilitating the determination of W_c . It should be noted that the Cockcroft–Latham fracture criterion is but one of many fracture criteria applicable to the current problem, see e.g. Wierzbicki et al. (2005). The Cockcroft–Latham criterion was chosen here because of its simplicity with respect to both formulation and calibration procedures (Reyes et al., 2009). Furthermore, it has been successfully used in previous studies of cast materials (Dørum et al., 2009; Dørum et al., 2009; Dørum et al., 2009).

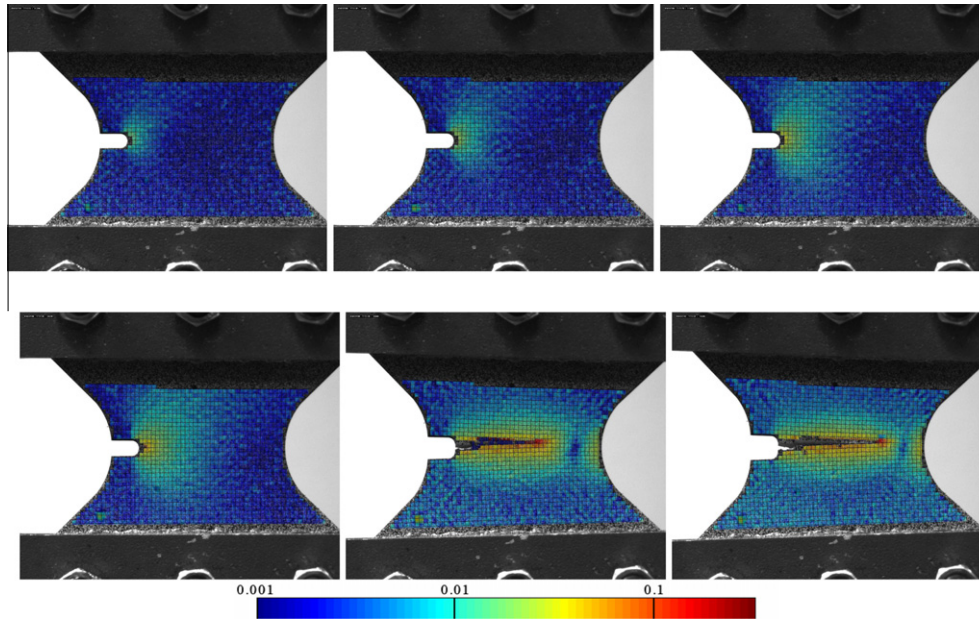


Fig. 12. Measured effective strain fields for a selection of images in a test for $\beta = 90^\circ$ (mode I). The strain fields are plotted on top of the recorded images in current configuration as logarithmic scaled colour maps.

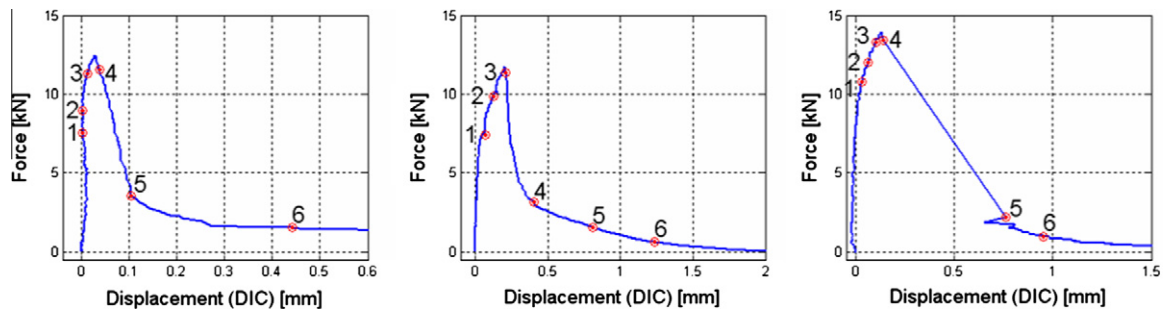


Fig. 13. Force–displacement curves from the experiments for (from left to right) $\beta = 0^\circ, 45^\circ$ and 90° . The corresponding strain maps in Figs. 10–12 are indicated on the force displacement curves with numbers 1–6.

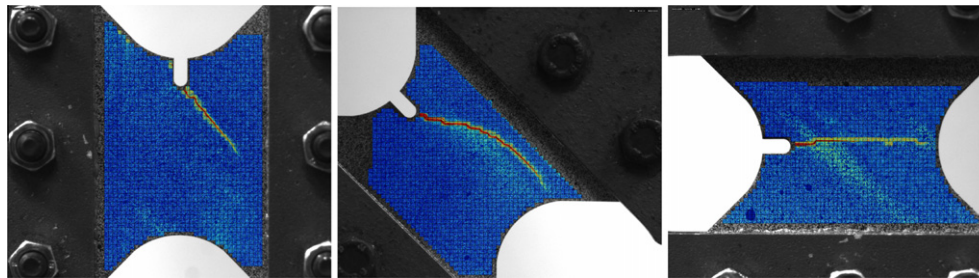


Fig. 14. Correlation residuals indicating crack paths in reference coordinates for (from left to right) $\beta = 0^\circ, 45^\circ$ and 90° . The correlation residual fields are plotted on top of the reference image (or un-deformed state) as colour maps.

To reduce the mesh-size sensitivity of the simulations with fracture, the non-local regularization available in LSTC (2003) was used (see e.g. Pijaudier-Cabot and Bāzant, 1987). To this end, the local values of the damage rate \dot{D} and the plastic strain rate $\dot{\epsilon}_z^p$ in the thickness direction of the profile were replaced by non-local values \bar{D} and $\bar{\epsilon}_z^p$ defined within the neighbourhood Ω_r , i.e.:

$$\bar{D}(\mathbf{x}_r) = \frac{1}{W_r} \int_{\Omega_r} w(\mathbf{x}_r - \mathbf{y}) \dot{D}(\mathbf{y}) d\Omega, \quad (12)$$

$$\bar{\epsilon}_z^p(\mathbf{x}_r) = \frac{1}{W_r} \int_{\Omega_r} w(\mathbf{x}_r - \mathbf{y}) \dot{\epsilon}_z^p(\mathbf{y}) d\Omega, \quad (13)$$

where

$$W_r = \int_{\Omega_r} w(\mathbf{x}_r - \mathbf{y}) d\Omega, \quad (14)$$

$$w(\mathbf{x}_r - \mathbf{y}) = \frac{1}{\left[1 + \left(\frac{\|\mathbf{x}_r - \mathbf{y}\|}{L}\right)^p\right]^q}. \quad (15)$$

Here, w is the non-local weight function, \mathbf{x}_r and \mathbf{y} are position vectors and the parameters L , p and q determine the shape of the weight function. The radius of the non-local domain Ω_r is taken as $L_{\max} = 1.5L$.

The reason for taking both damage D and through-thickness plastic strain ϵ_z^p as non-local variables is as follows. For thin-walled components under tension loading there are generally two different failure modes, namely local necking and fracture. When modelling such components with shell elements, local necking becomes, in addition to damage, severely mesh dependent because the shell elements fail to account for the stabilizing effect of stress triaxiality. It is therefore necessary to regularize both these variables to improve mesh convergence.

The fracture parameter W_c of an element is assumed to follow a modified weakest-link Weibull distribution in this study. The fracture probability of a material volume is given as

$$P(W) = 1 - \exp \left[- \left(\frac{V}{V_0} \right) \left(\frac{W}{W_{c0}} \right)^m \right], \quad (16)$$

where V is the volume of the element, V_0 is the scaling volume, W_{c0} is the scaling fracture parameter and m is the Weibull modulus. Consequently, the corresponding probability density function for the local material ductility reads

$$f(W_c) = \frac{dP}{dW} \Big|_{W=W_c} = \frac{m}{W_{c0}} \left(\frac{V}{V_0} \right) \left(\frac{W_c}{W_{c0}} \right)^{m-1} \exp \left[- \left(\frac{V}{V_0} \right) \left(\frac{W_c}{W_{c0}} \right)^m \right]. \quad (17)$$

To limit the local ductility of the material, an upper limit W_c^{\max} was introduced as an additional parameter (Dørum et al., 2009).

It is seen that the probability of fracture increases with increasing volume V , and in this sense the adopted fracture criterion accounts for size effects. It should be noted that size effects are important with respect to identification of fracture parameters for aluminium die-castings as demonstrated by Dørum et al. (2009), since the probability of testing a part of the material having a defect that initiates fracture increases with increasing volume. However, Dørum et al. (2009) show that the fracture modelling approach combining the Cockcroft–Latham fracture criterion with Weibull theory effectively handles size effects.

In the user-defined material model implemented in LS-DYNA, the scaling volume V_0 was taken as the volume of the gauge area of the tensile specimen, while V is the volume of the actual element. As the calibrated Weibull parameters rely on observed macroscopic failure, a minimum length scale is introduced to avoid simulating microcracks when the element lengths in the finite element models are very small. This is done by defining a non-local fracture parameter \bar{W}_c for each integration point in the finite element model as the minimum value of W_c within the neighbourhood Ω_r of radius L_{\max} , viz

$$\bar{W}_c(\mathbf{x}_r) = \min_{\|\mathbf{x}_r - \mathbf{y}\| \leq L_{\max}} W_c(\mathbf{y}). \quad (18)$$

Table 2 shows the Weibull parameters that were calibrated for Al-Si9MgMn-T1 in a previous work (Dørum et al., 2009). With respect to the non-local regularization, L was set equal to 2 mm with $p = 4$ and $q = 20$. Fig. 15 shows the bell shape of the weight function obtained using these parameter values. It is seen that the effective part of the non-local neighbourhood has a diameter similar to the thickness of the component. This is reasonable because local necking occurs at a length scale of the same order as the thickness.

In a previous work (Dørum et al., 2009) numerical simulations of the uniaxial tensile tests were carried out. It was found that the predicted engineering stress–strain curves from simulations

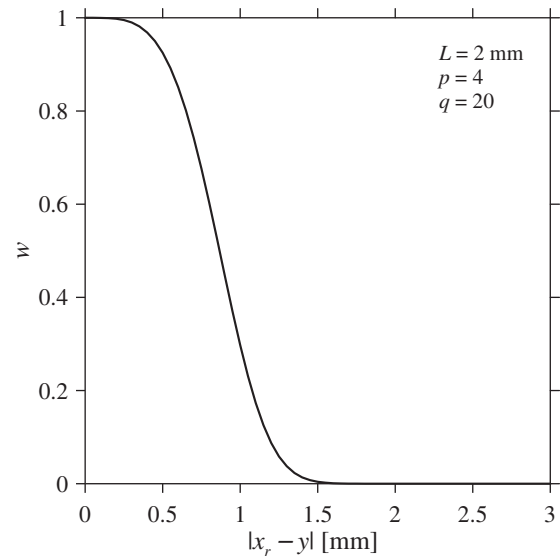


Fig. 15. Bell function used for non-local regularization with $L = 2$ mm, $p = 4$ and $q = 20$.

are very similar to the experimental curves. Numerical simulation of the uniaxial tensile test assuming homogeneous material properties and the ductility of the cast aluminium plates defined by the upper limit W_c^{\max} will overestimate the ductility in the uniaxial tensile test. Experimentally, the probability of reaching W_c^{\max} increases as the material volume decreases.

6. Numerical results

The modified Arcan tests were simulated in LS-DYNA using shell elements. First, a structured mesh with characteristic element lengths of 1.0 mm was created. This gave 1214 quadrilateral elements for the cast aluminium specimen. To examine the mesh-size sensitivity of the simulations, two refined meshes were made with element lengths equal to 0.5 and 0.25 mm, giving 5704 and 22,816 elements for the cast aluminium specimen, respectively. Second, meshes with the same characteristic lengths were generated using free quadrilateral meshing in LS-PREPOST 3.0. The corresponding number of elements for these arbitrary meshes are 1644, 6930 and 27559. In the following, the structured meshes are called M1–M3, while the arbitrary meshes are called A1–A3. Fig. 16 shows close-ups at the notch of the different meshes used in the simulations. Thus, the tests could now be simulated to evaluate the sensitivity of the predictions of fracture and crack propagation with respect to both mesh orientation and mesh density. An overview of the meshes used in the present work is provided in Table 3. It should be noted that shell elements cannot describe the slanted fracture seen in the experiments, cf. Fig. 9. However, we adopted shell elements here because we wanted to establish methods applicable for large-scale industrial applications and to evaluate the accuracy and robustness of this approach.

Fig. 17 shows predicted force–displacement curves obtained using meshes M1–M3 and A1–A3 when homogeneous material properties are assumed. From the Weibull distribution of fracture parameters, an average value of W_c can be calculated as a function of the volume of the material. As the stress and strain gradients are relatively steep in the cases studied here, the volume of the material where fracture is likely to initiate will be much smaller than the volume of the specimen gauge section used in calibration, but different for each load case. Further, as it is not straightforward to establish the size of the fracture-relevant volume, it has

Table 2
Weibull parameters.

V_0 (mm ²)	m	W_{c0} (MPa)	W_c^{\max} (MPa)
320	3.06	16.0	58

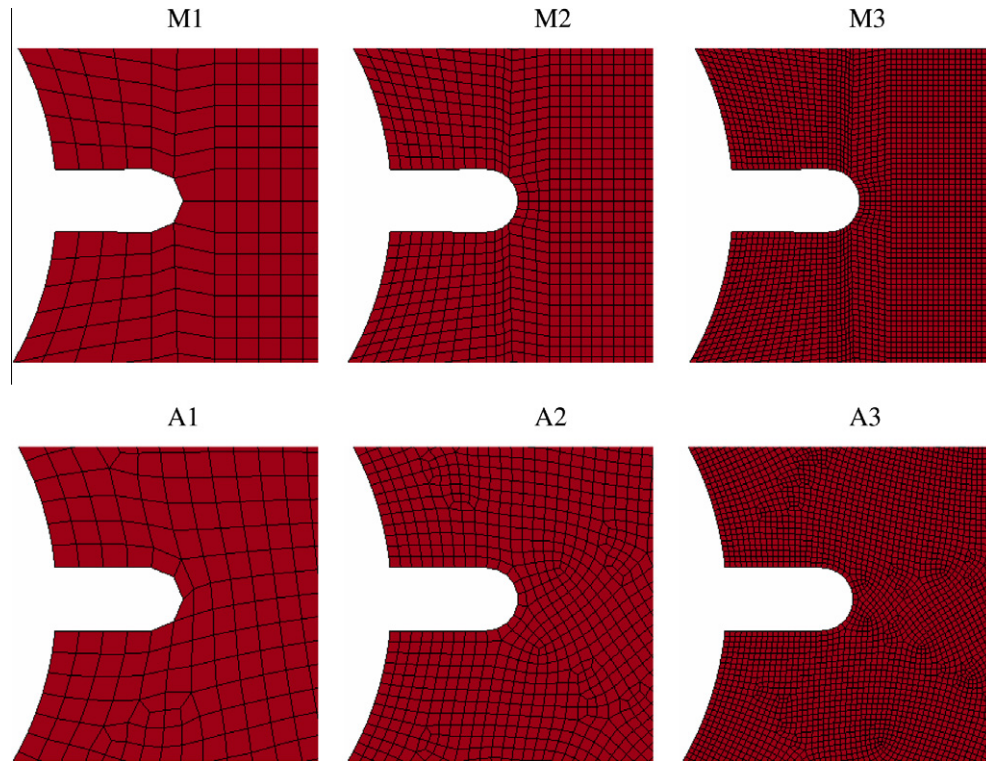


Fig. 16. The different meshes used to examine mesh-size sensitivity. Above, the structured meshing (M1–M3) and below, the automatic meshing (A1–A3).

Table 3
Finite-element meshes.

Meshing technique	Mesh identification	Number of elements	Characteristic element length (mm)
Structured meshing	M1	1214	1.0
	M2	5704	0.5
	M3	22,816	0.25
Automatic meshing	A1	1644	1.0
	A2	6930	0.5
	A3	27,559	0.25

been chosen to define the ductility of the cast aluminium plates by the upper limit $W_c = W_c^{\max} = 58$ MPa. This should lead to non-conservative estimates. The figure shows that with the adopted non-local regularization scheme, there is generally limited effect of mesh-size and mesh orientation on the predicted force–deformation curves. In the present study, local necking is of minor importance while the in-plane stress and strain gradients are steep. Therefore, mesh convergence mainly depends on the introduction of damage as a non-local variable. Simulations were also conducted without non-local regularization and then strong mesh sensitivity was observed. These results are not shown in the present study. The predicted force–deformation curves are in reasonable agreements with the experimental data until fracture occurs in the test, but with homogeneous material properties and the chosen value of W_c the ductility is over-predicted for all loading angles. The corresponding crack propagation paths for the two finest meshes A3 and M3 are given in reference configuration in Fig. 18. Some deviation between predicted and experimental crack paths is evident by comparing these plots to e.g. Fig. 9, but the overall agreement is reasonable. It is further noted that the crack width depends on the mesh-size in these simulations, since element erosion was adopted to propagate the crack.

To investigate the influence of using a probability distribution for fracture parameter, the three load cases were simulated with

the arbitrary mesh A3. The resulting force–deformation curves from three parallel simulations are plotted in Fig. 19 together with the representative experimental data. Significantly better estimates of the ductility are now obtained. We also get similar scatter in the simulated and experimental results. The significant drop in force level observed in one of the simulations for $\beta = 0^\circ$ is due to a considerable change in crack direction during fracture. Variations in crack paths also occur between parallel simulations in a similar way as seen experimentally. Note that the regularization leads to some areas where the crack width exceeds the characteristic element size due to the non-local averaging procedure.

Finally, Figs. 20–22 show the effective strain field $\varepsilon_{eff} = \varepsilon_{eff}(\mathbf{X}, t)$ from simulations for the three loading angles, adopting the fracture parameter as a random variable. It should be emphasized that the effective strain fields were obtained in exactly the same manner as in the experiments. This was done by importing nodal data from LS-DYNA into the in-house DIC software and using the formulas presented in Section 4. If compared to those obtained from the DIC measurements (Figs. 10–12), close correlation between the strain fields are seen even though some differences exist in the crack patterns and crack extension at similar force levels. It should, however, be kept in mind that these plots represent only one realization of the stochastic response for each loading case, and significant scatter has been shown to occur between replicate tests both experimentally and numerically. These plots show that both the displacement and strain fields in the modified Arcan tests can be accurately predicted using the described numerical approach.

7. Concluding remarks

In this paper, the quasi-static fracture behaviour of thin-walled cast aluminium components has been studied both experimentally and numerically.

Experimental tests were carried out using a modified Arcan set-up, making it possible to study fracture in modes I, II and

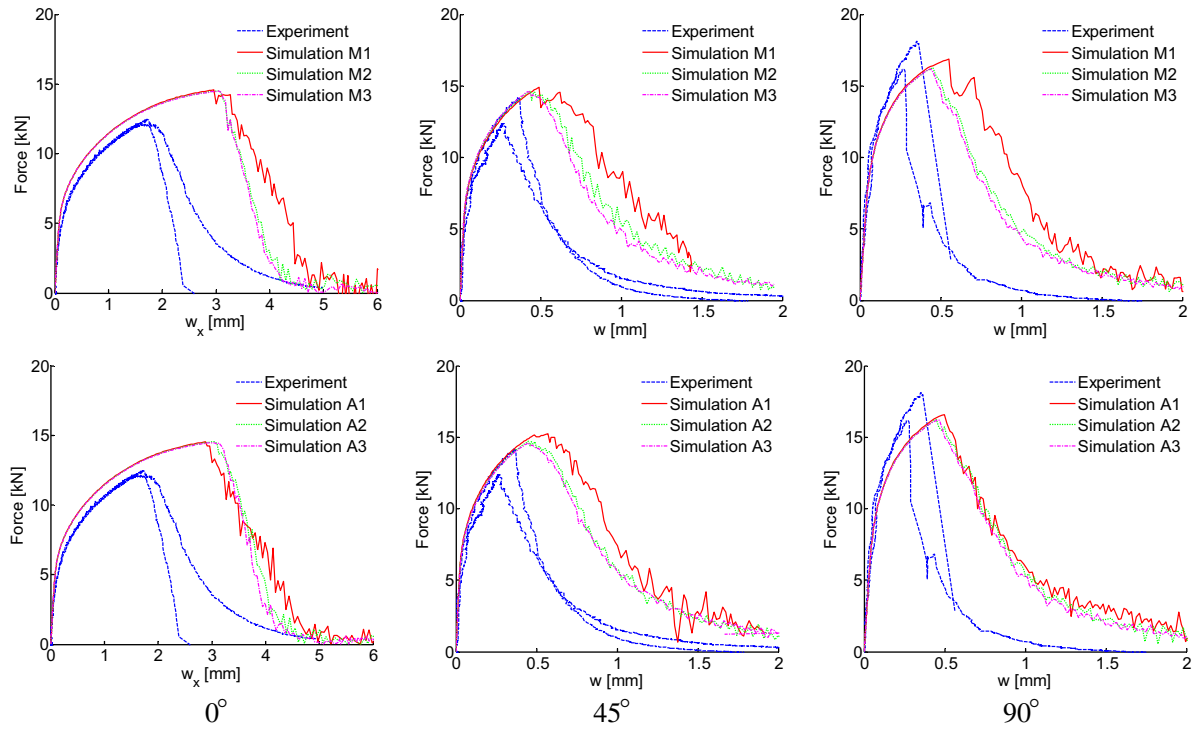


Fig. 17. Comparison of experimental and predicted force–deformation curves assuming homogeneous material properties. From left to right, $\beta = 0^\circ, 45^\circ$ and 90° .

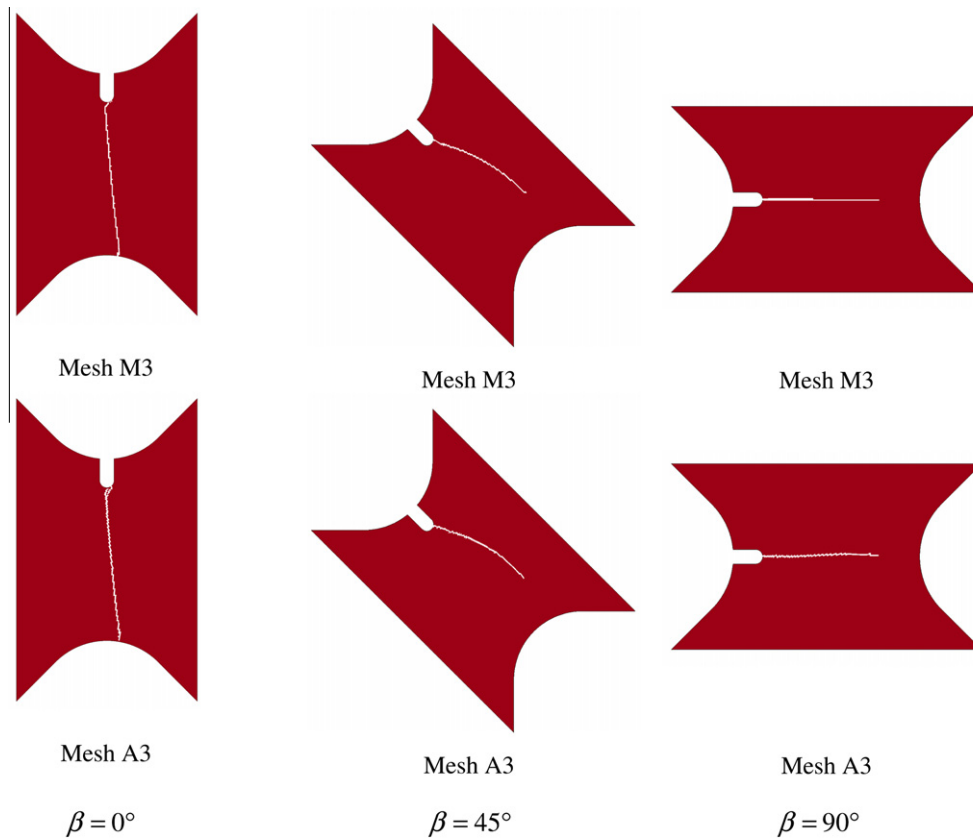


Fig. 18. Predicted crack propagation paths for the finest meshes M3 and A3. From left to right, $\beta = 0^\circ, 45^\circ$ and 90° . Homogeneous material properties are assumed.

mixed-modes. During testing, a digital camera was used to record a speckle-pattern on the surface of the sample. The recorded images

were post-processed using an in-house DIC software to obtain the displacement and strain fields in the sample. This software allows

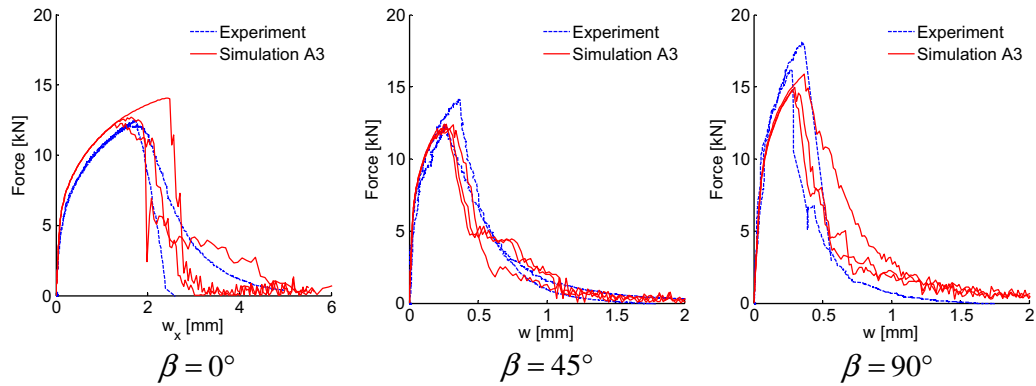


Fig. 19. Comparison of experimental and predicted force–deformation curves, adopting the fracture parameter as a random variable. From left to right, $\beta = 0^\circ$, 45° and 90° .

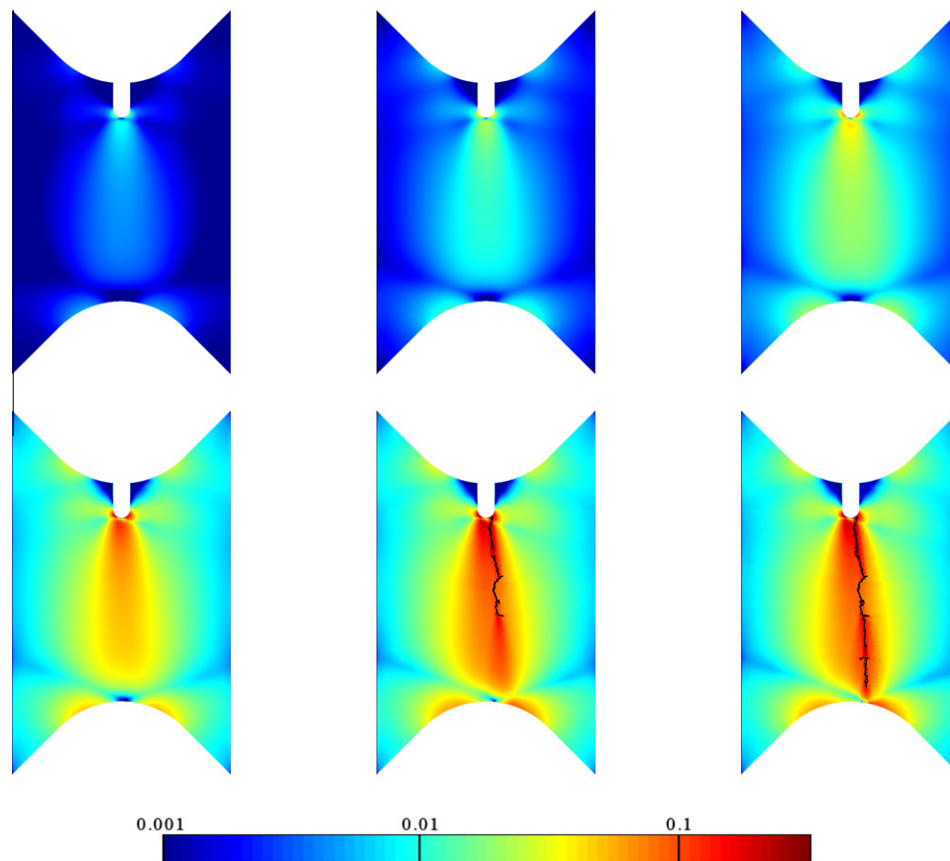


Fig. 20. Effective strain fields for $\beta = 0^\circ$ (mode II) from finite element analysis with the fracture parameter introduced as a random variable, plotted as logarithmic scaled colour maps. The model is plotted in the reference (or un-deformed) configuration.

for discontinuous displacement fields and thus makes it possible to establish the strain fields in the neighbourhood of a propagating crack.

Nonlinear finite element simulations were carried out using shell elements and an uncoupled continuous–discontinuous approach to describe damage, fracture and crack propagation. The classical J_2 flow theory was adopted to describe the material behaviour, while the damage evolution in the fracture process zone was computed according to the Cockcroft–Latham criterion. Element erosion was used to model crack propagation in the specimen. Since large variations in tensile ductility between parallel tests were found in a previous study, the fracture parameter was introduced as a random variable in the finite element simulations,

adopting a modified weakest-link Weibull distribution. Non-local regularization was adopted to reduce mesh-size sensitivity. To reveal the effect of mesh density and meshing technique on the force–displacement curves and crack propagation, several different meshes were used in the simulations. The numerical results were finally compared to the measured data.

It was found that the force–deformation curves, the fracture modes and the effective strain fields of the modified Arcan tests were predicted with reasonable accuracy using the described numerical approach. Without non-local regularization strong mesh sensitivity was found, while failing to account for the probability distribution of the fracture parameter led to non-conservative estimates on the ductility of the notched butterfly test specimen with

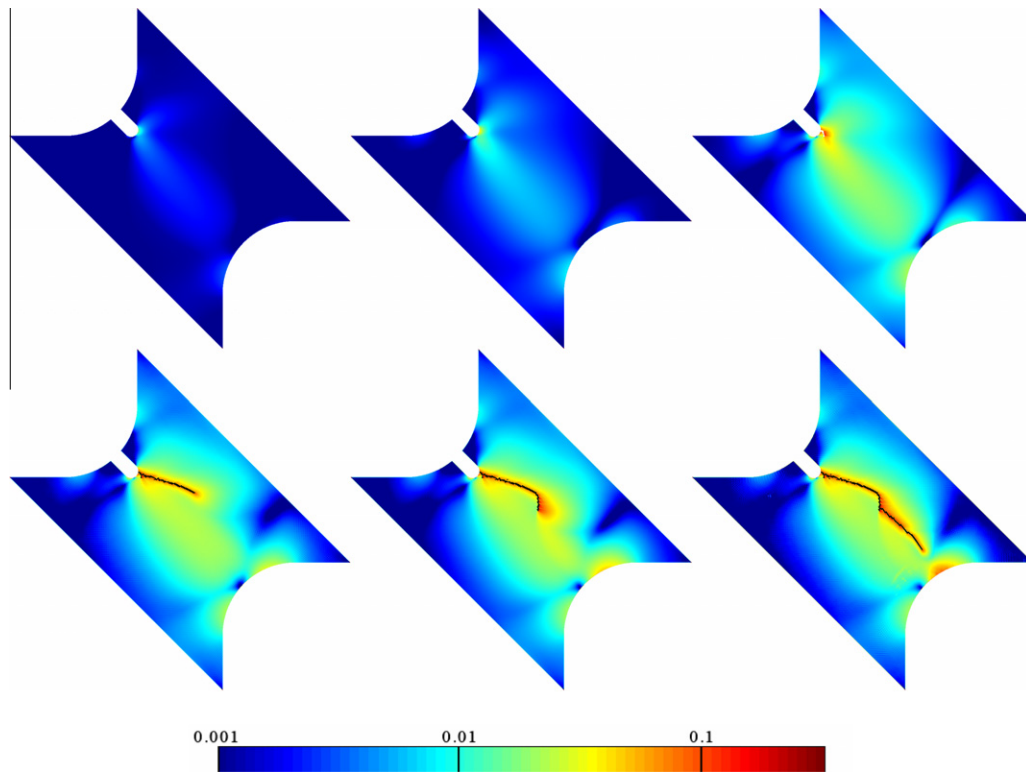


Fig. 21. Effective strain fields for $\beta = 45^\circ$ (mixed-mode) from finite element analysis with the fracture parameter introduced as a random variable, plotted as logarithmic scaled colour maps. The model is plotted in reference (or un-deformed) configuration.

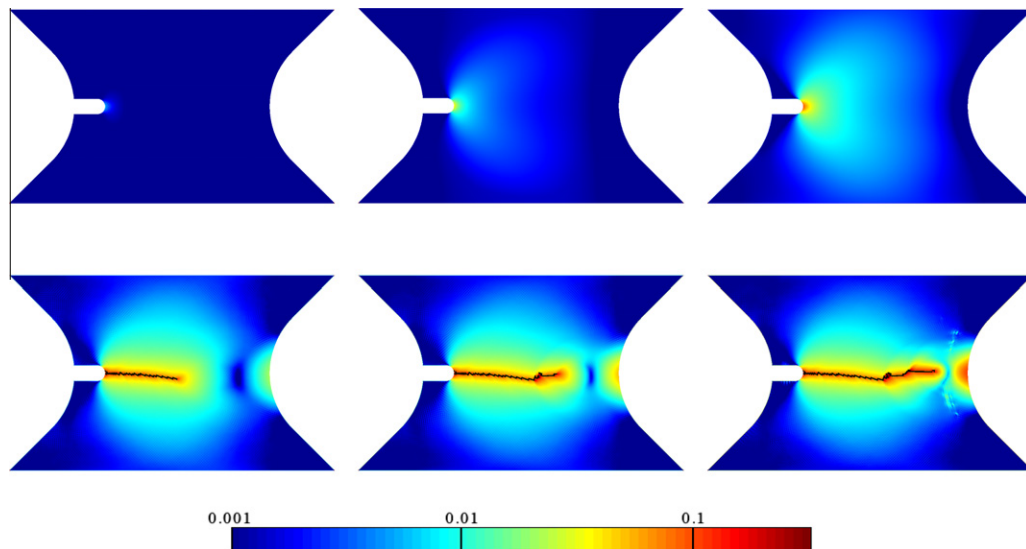


Fig. 22. Effective strain fields for $\beta = 90^\circ$ (mode I) from finite element analysis with the fracture parameter introduced as a random variable, plotted as logarithmic scaled colour maps. The model is plotted in reference (or un-deformed) configuration.

the current choice of the homogeneous fracture parameter. Some differences were also seen between the experimental and predicted crack paths. The use of element erosion to propagate the crack forces it to follow the element mesh, and thus imposes a constraint on the solution. For this reason use of arbitrary meshing may provide improved results over structured meshing. However, there were also marked differences in the crack paths between replicate tests in both the experiments and the simulations. Even if there are limitations in the proposed modelling approach, the results are believed to be satisfactory for applications to large-scale simulations of industrially relevant problems.

Acknowledgement

The financial support of this work from the Structural Impact Laboratory (SIMLab), Centre for Research-based Innovation (CRI) at the Norwegian University of Science and Technology (NTNU), is gratefully acknowledged.

References

- Amstutz, B.E., Sutton, M.A., Dawicke, D.S., Newman, J.C., 1996. An experimental study of CTOD for mode I/mode II stable crack growth in thin 2024-T3 aluminium specimens. *Fract. Mech. ASTM* 26, 256–271.

- Amstutz, B.E., Sutton, M.A., Dawicke, D.S., Boone, M.L., 1997. Effects of mixed mode I/II loading and grain orientation on crack initiation and stable tearing in 2024-T3 aluminium. *Fatigue Fract.* 27, 217–224.
- Arcan, M., Hashin, Z., Voloshin, A., 1978. Method to produce uniform plane stress states with applications to fibre-reinforced materials. *Exp. Mech.* 18, 141–146.
- Besnard, G., Hild, F., Roux, S., 2006. Finite-element displacement fields analysis from digital images: application to Portevin-le Châtelier bands. *Exp. Mech.* 46, 789–803.
- Campbell, J., 1988. Thin wall castings. *Mater. Sci. Technol.* 4, 194–204.
- Campbell, J., 2005. Shape Casting – The John Campbell Symposium. In: TMS Conference, pp. 3–12.
- Cockcroft, M.G., Latham, D.J., 1968. Ductility and workability of metals. *J. Inst. Met.* 96, 33–39.
- Dørum, C., Hopperstad, O.S., Berstad, T., Dispinar, D., 2009. Numerical modelling of magnesium die-castings using stochastic fracture parameters. *Eng. Fract. Mech.* 76, 2232–2248.
- Dørum, C., Laukli, H.I., Hopperstad, O.S., 2009. Through-process numerical simulations of the structural behaviour of Al–Si die-castings. *Comput. Mater. Sci.* 46, 100–111.
- Dørum, C., Laukli, H.I., Hopperstad, O.S., Langseth, M., 2009. Structural behaviour of Al–Si die-castings: experiments and numerical simulations. *Eur. J. Mech. A. Solids* 28, 1–13.
- Fagerholt, E., Børvik, T., Hopperstad, O.S., in preparation. Handling of crack propagation in specimens using two-dimensional digital image correlation (2D-DIC).
- Gokhale, A.M., Patel, G.R., 2005. Analysis of variability in tensile ductility of a semi-solid metal cast A356 Al-alloy. *Mater. Sci. Eng. A* 392, 184–190.
- Gokhale, A.M., Patel, G.R., 2005. Origins of variability in the fracture-related mechanical properties of a tilt-pour-permanent mould cast Al-alloy. *Scr. Mater.* 52, 237–241.
- Gourlay, C.M., Laukli, H.I., Dahle, A.K., 2007. Defect band characteristics in Mg–Al and Al–Si high-pressure die castings. *Metall. Mater. Trans. A* 38A, 1833–1844.
- Gurson, A.L., 1977. Continuum theory of ductile rupture by void nucleation and growth. Part I: Yield criteria and flow rule for porous ductile media. *J. Eng. Mater. Technol.* 99, 1–15.
- Helm, J.D., 2008. Digital image correlation for specimens with multiple growing cracks. *Exp. Mech.* 48, 753–762.
- Laukli, H.I., Gourlay, C.M., Dahle, A.K., 2005. Effects of Si content on defect band formation in hypoeutectic Al–Si die castings. *Mater. Sci. Eng. A*, 92–97.
- Laukli, H.I., Gourlay, C.M., Dahle, A.K., 2005. Migration of crystals during the filling of semi-solid castings. *Metall. Mater. Trans. A* 36A, 805–818.
- Lemaitre, J., 1992. *A Course on Damage Mechanics*. Springer-Verlag, Berlin.
- LSTC, 2003. *LS-DYNA Keyword User's Manual*, Version 970. Livermore Software Technology Corporation.
- LS-PREPOST 3.0. Available from: <<http://www.lstc.com/lsp>> (accessed 07.01.10).
- Mediavilla, J., Peerlings, R.H.J., Geers, M.D.G., 2006. A robust and consistent remeshing-transfer operator for ductile fracture simulations. *Comput. Struct.* 84, 604–623.
- Moës, N., Dolbow, J., Belytschko, T., 1999. A finite element method for crack growth without remeshing. *Int. J. Numer. Methods Eng.* 46, 131–150.
- Mohr, D., Henn, S., 2007. Calibration of stress-triaxiality dependent crack formation criteria: a new hybrid experimental method. *Exp. Mech.* 47, 805–820.
- Needleman, A., 1990. An analysis of decohesion along an imperfect interface. *Int. J. Fract.* 42, 21–40.
- Pijaudier-Cabot, G., Băzant, Z.P., 1987. Nonlocal damage theory. *J. Eng. Mech.* 113, 1512–1533.
- Rastogi, P.K. (Ed.), 2000. *Photomechanics*. Springer, Berlin, Germany.
- Rèthorè, J., Hild, F., Roux, S., 2007. Shear-band capturing using a multiscale extended digital image correlation technique. *Comput. Methods Appl. Mech. Eng.* 196, 5016–5030.
- Reyes, A., Eriksson, M., Lademo, O.-G., Hopperstad, O.S., Langseth, M., 2009. Assessment of yield and fracture criteria using shear and bending tests. *Mater. Des.* 30 (3), 596–608.
- Rousselier, G., 1987. Ductile fracture models and their potential in local approach of fracture. *Nucl. Eng. Des.* 105, 97–111.
- Scheider, I., Brocks, W., 2006. Cohesive elements for thin-walled structures. *Comput. Mater. Sci.* 37, 101–109.
- Song, J.-H., Wang, H., Belytschko, T., 2008. A comparative study on finite element methods for dynamic fracture. *Comput. Mech.* 42, 239–250.
- Teng, X., Mae, H., Bai, T., Wierzbicki, T., 2008. Statistical analysis of ductile fracture properties of an aluminium casting. *Eng. Fract. Mech.* 75, 4610–4625.
- Voloshin, A., Arcan, M., 1980. Failure of unidirectional fiber-reinforced materials – new methodology and results. *Exp. Mech.* 20 (8), 280–284.
- Weibull, W., 1951. A statistical distribution function of wide applicability. *J. Appl. Mech.* 18, 293–297.
- Wierzbicki, T., Bao, Y., Lee, Y.-W., Bai, Y., 2005. Calibration and evaluation of seven fracture models. *Int. J. Mech. Sci.* 47, 719–743.